Engineering Optimization
Publication details, including instructions for authors and subscription information:
http://www.tandfonline.com/loi/geno20

A comprehensive preference-based optimization framework with application to high-lift aerodynamic design

Robert Carrese [a] , Hadi Winarto [a] , Xiaodong Li [a] , András Sóbester [b] & Samuel Ebenezer [c]

[a] School of Aerospace Mechanical and Manufacturing, RMIT University, Melbourne, VIC, Australia

[b] Computational Engineering and Design, University of Southampton, Highfield, Southampton, UK

[c] Program Development Company LLC., Kodihalli, Bangalore, India

Version of record first published: 08 Feb 2012.

To cite this article: Robert Carrese, Hadi Winarto, Xiaodong Li, András Sóbester & Samuel Ebenezer (2012): A comprehensive preference-based optimization framework with application to high-lift aerodynamic design, Engineering Optimization, 44:10, 1209-1227

To link to this article: http://dx.doi.org/10.1080/0305215X.2011.637558

Engineering Optimization
Vol. 44, No. 10, October 2012, 1209–1227

A comprehensive preference-based optimization framework with application to high-lift aerodynamic design

Robert Carrese[a]*, Hadi Winarto[a], Xiaodong Li[a], András Sóbester[b] and Samuel Ebenezer[c]

[a]*School of Aerospace Mechanical and Manufacturing, RMIT University, Melbourne, VIC, Australia;*
[b]*Computational Engineering and Design, University of Southampton, Highfield, Southampton, UK;*
[c]*Program Development Company LLC., Kodihalli, Bangalore, India*

(*Received 18 May 2011; final version received 11 October 2011*)

An integral component of transport aircraft design is the high-lift configuration, which can provide significant benefits in aircraft payload-carrying capacity. However, aerodynamic optimization of a high-lift configuration is a computationally challenging undertaking, due to the complex flow-field. The use of a designer-interactive multiobjective optimization framework is proposed, which identifies and exploits preferred regions of the Pareto frontier. Visual data mining tools are introduced to statistically extract information from the design space and confirm the relative influence of both variables and objectives to the preferred interests of the designer. The framework is assisted by the construction of time-adaptive Kriging models, which are cooperatively used with a high-fidelity Reynolds-averaged Navier–Stokes solver. The successful integration of these design tools is facilitated through the specification of a reference point, which can ideally be based on an existing design configuration. The framework is demonstrated to perform efficiently for the present case-study within the imposed computational budget.

Keywords: high-lift aerodynamics; multiobjective optimization; data mining; preferences; Kriging

1. Introduction

To achieve sufficient low-speed performance without compromising cruise performance requires a fairly sophisticated high-lift configuration (van Dam 2002). The primary goal of an aerodynamic high-lift system is to increase payload capacity and reduce take-off and landing distances by maximizing the lift coefficient for a given angle of incidence, without the onset of massive flow separation (Smith 1975). Studies confirm that relatively small changes in the aerodynamic performance of a high-lift system potentially translate to major benefits in aircraft payload-carrying capacity and performance (Garner *et al.* 1991). For this reason, high-lift aerodynamic and system design remain at the forefront of aerospace research.

For a typical high-lift configuration design, involving a forward (slat) element and an aft (flap) element, the flow field is physically complex due to the element interactions (Smith 1975; van Dam 2002). Combined with the intricacy of system support and actuation, this has traditionally led to an

---

*Corresponding author. Email: robert.carrese@rmit.edu.au

ISSN 0305-215X print/ISSN 1029-0273 online

http://dx.doi.org/10.1080/0305215X.2011.637558
http://www.tandfonline.com

experiment intensive development process. However, due to the recent development of numerical modelling and computing facilities, computational fluid dynamics (CFD) are superseding physical experimentation design methods (Rumsey and Ying 2002). In particular, the significant progress achieved in synthesizing automated optimization tools and high-fidelity CFD has significantly reformed the aerodynamic design philosophy (Kim *et al.* 2004; Keane and Nair 2005). Innovative design methods have since been proposed, *e.g.* by drawing on evolutionary theory (Quagliarella and Vicini 2001; Kanazaki *et al.* 2006), the collective intelligence of a swarm (Khurana and Winarto 2010), or the ability of a neural network to detect patterns in complex input–output data relationships (Greenman and Roth 1999), etc. These evolutionary techniques are formulated to find the most optimal system configuration to suit the preferences of the designer, in the shortest time possible.

High-lift configuration design is a multiobjective optimization problem, where trade-offs are sought between several different goals or design conditions. Such problems present an interesting challenge to evolutionary methodologies and follow the generic form:

$$\min_{\mathbf{x}\in S} f(\mathbf{x}) = \{f_1(\mathbf{x}), \ldots, f_m(\mathbf{x})\} \quad f_i : S \to \mathbb{R}, \tag{1}$$

where $\mathbf{x}$ represents a decision vector of n inputs $\mathbf{x} = \{x_1, \ldots, x_n\}$ subject to the design space $S \in \mathbb{R}^n$ bounded by the lower and upper limits $\mathbf{x}_{\min}$ and $\mathbf{x}_{\max}$, respectively. The vector f represents m objectives, that generally conflict if the problem is well formed. The aim of multiobjective optimization is to identify trade-off (or Pareto optimal) solutions which are in the preferred interests of the designer. Methods for solving multiobjective problems are therefore characterized by how the designer preferences are articulated (Marler and Arora 2004). Despite the merits of the increasingly popular evolutionary multiobjective methods (Deb 2001), their direct application to high-fidelity design is not very practical and computationally demanding (Keane and Nair 2005). Fonseca and Fleming (1995) however argue that their most attractive aspect is the intermediate information generated which can be exploited by the designer to refine preferences and improve convergence. There has thus been an increasing interest in coupling classical interactive methods to evolutionary multiobjective algorithms as an intuitive way of specifying designer preferences and identifying solutions of interest to the designer (Fonseca and Fleming 1998; Deb and Sundar 2006; Rachmawati and Srinivasan 2006; Wickramasinghe and Li 2008).

In an earlier study (Carrese *et al.* 2011a), it was demonstrated that, through the use of designer preferences, the computational burden of exploring the entire Pareto frontier is alleviated. The design algorithm was aided by a reference point which is projected onto the Pareto landscape by the designer to identify solutions of interest. Unlike conventional interactive methods which make explicit reference to a target design (*e.g.* goal programming, see Marler and Arora 2004), the reference point expresses the designer's preferred level of *compromise*, which can ideally be based on an existing design or reflect the ideal trade-off. The algorithm is guided by this information to confine its search to the preferred region of the Pareto front. The concept of preference-based optimization was developed further to incorporate the use of surrogates by Carrese *et al.* (2011b). It was demonstrated that by replacing each objective function with a time-adaptive Kriging model, a significant reduction in the computational evaluations was achieved, notwithstanding the apparent discontinuities in the objective landscapes. The reference point criterion introduced to locally update the Kriging models was shown to be adept at filtering out solutions which disrupt or deviate from the optimal search path dictated by the reference point.

In conjunction with intricate optimization heuristics, the use of design space visualization and data mining techniques has also progressively increased (Obayashi and Sasaki 2003; Jeong *et al.* 2005; Khurana and Winarto 2010). Such methodologies are applied to extract useful information on the relationship between the design space and the objective space. However when confronted with a multi-dimensional design space and conflicting goals, identifying and isolating the case-specific information that suits the intended application can be challenging. In this article, a series of visual data mining techniques used for pre-optimization variable screening and post-optimization trade-off visualization is presented. It is demonstrated that extracting case-specific information from the visualization analyses, based on the preferred interests of the designer, is facilitated through the reference point. Variable influence and interaction, as well as important factors which drive the design are easily identified. Such methods simplify a seemingly complex problem, allowing informed decisions to be made which may facilitate the optimization process.

These design tools are consolidated to develop an efficient framework for a two-dimensional high-lift configuration design scenario. Integration of the framework is entirely achieved through the use of a reference point distance metric which provides a scalar measure of the preferred interests of the designer. The implementation of designer preferences similarly allows the scale of the design space to be reduced, confining it to the interests reflected by the designer. The cooperative use of time-adaptive Kriging models allows for the use of a high-fidelity Reynolds averaged Navier–Stokes (RANS) solver, which accurately portrays the flow field due to interactions between the airfoil elements. The complex geometrical configurations are meshed through a multi-block structured gridding technique, which ensures quality structured grids for efficient convergence rates. Data mining techniques are used to visualize preferred trade-offs and quantify the driving influence of variables on the objective landscapes.

2. Problem formulation

High-lift configuration design is a highly multi-disciplinary process. For the present study, the problem is simplified to a two-dimensional aerodynamic optimization of a high-lift configuration. This simplification allows for a higher-fidelity solver, providing an interesting challenge to the proposed algorithm. The baseline three-element configuration for this optimization study is selected as the McDonnell-Douglas 30P/30N, shown in Figure 1. The 30P/30N configuration has already been highly optimized for maximum lift. Wind-tunnel measurements have been extensively performed for this configuration (Ying *et al.* 1999), and the results of many CFD computations for this geometry have been reported using a variety of numerical schemes (Rogers *et al.* 1994; Rumsey *et al.* 1998).

The variables used in the optimization study are the relative positions of the slat and flap components. These variables measure the gap, overlap and deflection angle relative to the main component. For the present study, relative positions of the slat and flap are specified indirectly, through $\pm x/c$ and $\pm y/c$ directional translations, and rotation $\pm\theta$. In these measurements, c refers to the clean airfoil chord with retracted flap and slat. In this way, the design variables are geometrically independent and their relative influence on the design space is easily identifiable. The design variables are initialized relative to the position of the original configuration. Figure 2 illustrates the translational and rotational displacement of the slat and flap components.

The proficiency of the proposed framework is demonstrated by maximizing the lift generated on the 30P/30N configuration at various design conditions, motivated by the work of Ying *et al.*

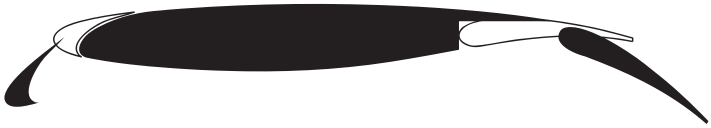

Figure 1. The MDC 30P/30N configuration with deployed slat (forward) and flap (aft) components.

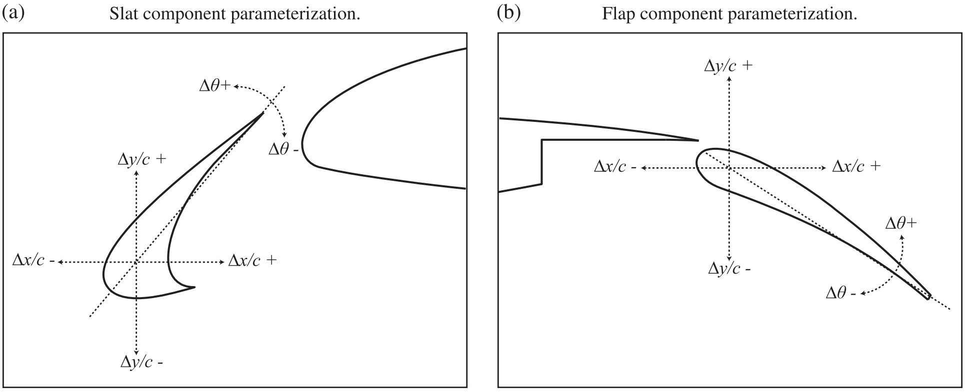

Figure 2. Parameterization variables for high-lift configuration.

Table 1. Design variable ranges for the optimization study.

Parameter	Description	Lower bound	Upper bound
Δx_{S}	Slat translation, $\Delta x/c$	−0.04	0.01
Δy_{S}	Slat translation, $\Delta x/c$	−0.03	0.04
$\Delta \theta_{\mathrm{S}}$	Slat rotation, $\Delta \theta$	−10°	10°
Δx_{F}	Flap translation, $\Delta x/c$	−0.02	0.04
Δy_{F}	Flap translation, $\Delta x/c$	−0.07	0.005
$\Delta \theta_{\mathrm{F}}$	Flap rotation, $\Delta \theta$	−10°	10°

(1999). All simulations are performed at a Reynolds number $\mathrm{Re}_c = 9 \times 10^6$ and Mach number $M = 0.2$. Three objectives are formulated for the problem, which are $f_1 = \min(1/C_{\mathrm{l}})$ and $f_2 = \min(C_{\mathrm{d}}/C_{\mathrm{l}})$ at $\alpha = 8°$, and $f_3 = \min(1/C_{\mathrm{l}})$ at $\alpha = 19°$, where C_{l} and C_{d} are the configuration lift and drag coefficient, respectively. The objectives f_1 and f_2 are optimized at an angle of incidence $\alpha = 8°$, typical of an approach configuration. The objective f_3 is optimized at an angle $\alpha = 19°$, nearing the angle where maximum lift is generated. Neither objective is discontinuous, but the third objective is highly nonlinear, as some configurations will lead to premature separation and stall. The boundaries of the design space are selected such that there is a smooth transition of the grid and do not result in any infeasible configurations (*e.g.* component intersection, etc.). The design variable ranges are shown in Table 1.

2.1. *Multi-block grid*

Due to the complexity of the geometry, most methods for high-lift configurations are typically based on unstructured grids or overset grids (Vatsa *et al.* 1994). These strategies are optimal for complex geometries, yet the computational efficiency and accuracy is poor relative to an orthogonally structured mesh. In this study, the block-structured grid generator GRIDPRO™ is utilized. The grid topology is divided into a number of many-to-one elementary blocks, which allows for accurate meshing of geometry, without the need to propagate dense grids to the computational far-field. Figure 3 illustrates a partial view of the grid topology generated for this problem.

The O-grid topology consists of 234 blocks, resulting in a total mesh size of approximately 80,000 elements. The far-field boundary extends $20c$ radially from the origin. The grid is algebraically clustered at the surface where the first grid point has a y-plus magnitude of $O(1)$, which is critical for adequate resolution of the boundary layer. It is shown in Figure 3 that there is a rather dense topology in regions of interest and the topology around the trailing edges of each

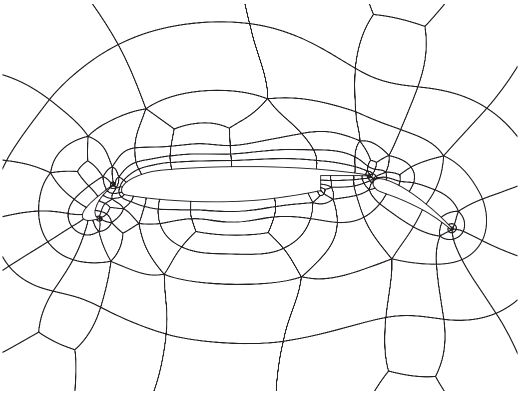

Figure 3. Multi-block grid topology generated for the 30P/30N configuration.

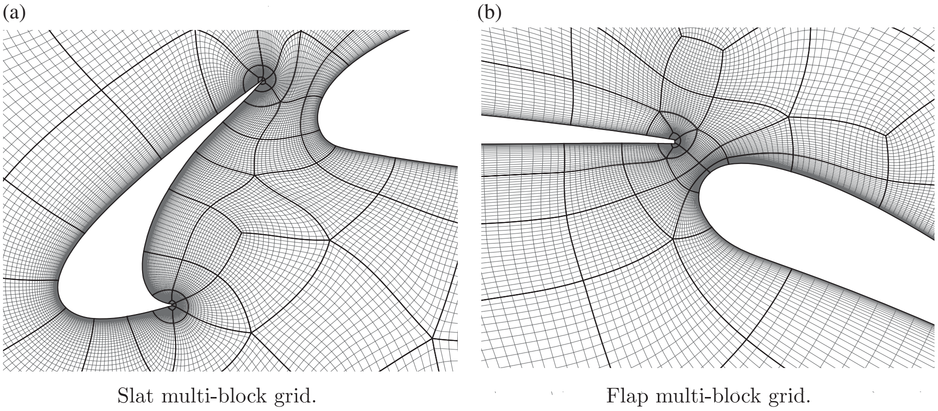

Slat multi-block grid.

Flap multi-block grid.

Figure 4. Partial close-up views of the multi-block grid.

component are mapped to an interior circular surface, in order to preserve orthogonality. Shown in Figure 4 is a close-up view of the slat and flap grids. During the optimization process, rather than regenerating a new topology, the surface and surrounding topological grid is translated and rotated according to the design variable notation.

2.2. *Flow solver*

Significant progress in formulating a theoretical basis for high-lift aerodynamics was pioneered by the work of Smith (1975). The circulation of a forward element or the slat effect reduces the leading edge suction peak, thus delaying separation. The trailing element however induces a circulation effect on the forward element which tends to increase the loading or lift generated. These flow phenomena are predominantly inviscid, yet viscous effects also arise due to the individual wakes from each element. While wakes reduce the pressure peak of trailing elements, they often tend to merge with the boundary layer of the trailing element resulting in a thicker shear layer, termed a confluent boundary layer, increasing the likelihood of separation.

To portray each of these flow phenomena, a high-fidelity flow solver is essential. In this study, the general purpose finite volume code ANSYS FLUENT™ is used. The compressible steady-state RANS

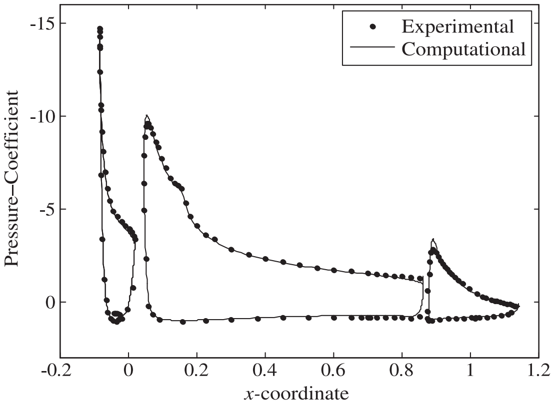

Figure 5. Comparison of surface C_p plots for the 30P/30N configuration at $\mathrm{Re} = 9 \times 10^6$, $\alpha = 19°$.

equations are solved with the implicit pressure-based scheme using second-order upwind spatial discretization and SIMPLE (Semi-Implicit Method for Pressure-Linked Equations) pressure–velocity coupling. In the interest of robust and efficient convergence rates, a full multi-grid (FMG) initialization scheme is employed, with coarsening of the grid to 100 cells. In the FMG initialization process, the Euler equations are solved using a first-order discretization scheme to obtain a flowfield approximation before submitting to the full iterative calculation. The one-equation Spalart–Allmaras turbulence closure model is selected to compute the eddy viscosity (Spalart and Allmaras 1992). The advantage of this model over two-equation turbulence models is that the turbulence equation is solved locally and its robust convergence rate makes it suitable for aerodynamic flows over complex geometries. Presented in Figure 5 is the accuracy of the computational flow solver compared to experimental data acquired from the NASA Langley Research Center (Ying *et al.* 1999). Fairly good agreement is observed across the entire geometry albeit the suction peaks predicted by the computational solver are marginally higher.

3. Optimization algorithm

The principal argument of this research is that, for most design applications, to explore the entire Pareto front is often unnecessary and the computational burden can be alleviated by considering the immediate interests of the designer. Drawing on this concept, a preference-based swarm algorithm is proposed, where a designer-driven distance metric is used to scalar quantify the success of a solution. The swarm is guided by this information to confine its search and focus exclusively on the preferred region of the Pareto front as dictated by a reference point or the preferred compromise. The reader is encouraged to follow the user-preference multiobjective particle swarm optimization (UP-MOPSO) algorithm description in previous articles (Carrese *et al.* 2011a,b), including a discussion on the swarm dynamics and topology. For the present article, the discussion is limited to the important components of the algorithm.

3.1. *Population update*

Particle swarm optimization (PSO) was introduced by Kennedy and Eberhart (2001) and is derived from the social-psychological tendency of individuals to learn from previous experience and emulate the success of others. Particles are represented by n-dimensional vectors $\mathbf{x}_i$ and $\mathbf{v}_i$, which are the ith particle position and velocity, respectively. From the performance rating provided by the objective solver, particles identify and exploit promising areas of the design space via coordinated movement. PSO is praised for its efficient convergence rate (Trelea 2003), and its success for single-objective optimization problems has since been reflected in the multiobjective community (Sierra and Coello 2006).

Following the work of Clerk and Kennedy (2002), the *i*th particle of the swarm is accelerated towards its personal best position, $\mathbf{p}_i$, and the global (or neighbourhood) best position, $\mathbf{p}_g$. The particle velocity magnitude is initialized randomly in the interval $[0, \mathbf{x}_{\max} - \mathbf{x}_{\min}]$. Half of the population's direction is reversed by setting the velocity to negative according to a coin toss. The updated position and velocity vectors at time $t + 1$ are given by the following two equations:

$$\mathbf{v}_{i,(t+1)} = \chi \left[\mathbf{v}_{i,(t)} + \mathbf{R}_1[0, \varphi_1] \otimes \left(\mathbf{p}_{i,(t)} - \mathbf{x}_{i,(t)}\right) + \mathbf{R}_2[0, \varphi_2] \otimes \left(\mathbf{p}_{g,(t)} - \mathbf{x}_{i,(t)}\right)\right] \tag{2}$$

$$\mathbf{x}_{i,(t+1)} = \mathbf{x}_{i,(t)} + \mathbf{v}_{i,(t+1)}, \tag{3}$$

where $\mathbf{R}_1[0, \varphi_1]$ and $\mathbf{R}_2[0, \varphi_2]$ are two functions returning a vector of uniform random numbers in the range $[0, \varphi_1]$ and $[0, \varphi_2]$, respectively. The constants φ_1 and φ_2 are set to $\varphi/2$ where $\varphi = 4.1$. The constriction factor χ applies a dampening effect as to how far the particle explores within the search space, given as $\chi = 2/|2 - \varphi - \sqrt{\varphi^2 - 4\varphi}|$.

3.2. *Reference point integration*

A multiobjective particle swarm optimization variant is developed which utilizes a reference point to provide additional guidance to the swarm to identify preferred solutions. At each time-step, the best representative non-dominated front found by the particles is stored within an elitist archive (Deb 2001). Additional guidance in selecting candidates is provided by a reference point distance metric, following the work of Wickramasinghe and Li (2008). The reference point $\mathbf{z}$ is used to construct a distance metric to be minimized for $\mathbf{x} \in S$, such that

$$d_z(\mathbf{x}) = \max_{i=1:m} \left\{(f_i(\mathbf{x}) - z_i)\right\}, \tag{4}$$

where z_i is the *i*th component of the reference point. A solution $\mathbf{x}^*$ is therefore *preferred* to a solution $\mathbf{x}$ if the condition $d_z(\mathbf{x}^*) < d_z(\mathbf{x})$ is satisfied. The distinguishing feature of the reference point distance metric over the mathematical Euclidean distance is that solutions do not converge to the reference point, but rather on the preferred region of the Pareto front as dictated by the optimal search path. Since the designer generally has no prior knowledge of the topology and location of the Pareto front, a reference point may be ideally placed in any feasible or infeasible region. Figure 6 illustrates the multiobjective swarm algorithm guided by the reference point for the ZTD (Zitzler *et al.* 2000) and DTLZ (Deb *et al.* 2005) test function suite.

The reference point draws on the experience of the designer to express a feasible compromise, rather than specific target values or goals. Similarly, the distance metric ranks the success of a particle using one single scalar, instead of an array of objective values. At each population update, archived solutions are first sorted based on the metric d_z, of which the highest ranking solutions are selected as candidates for leadership. Each swarm particle is then randomly assigned to a candidate, which is the respective global leader. This concept promotes search diversity and provides the necessary selection pressure for particles to converge towards the preferred region dictated by the reference point compromise, rather than a single point. To maintain high selection pressure on archive members, a limited number of solutions are permitted for entry. If the limit is breached, lowest ranked solutions are removed. The solution spread along the Pareto front is controlled by δ which is the maximum variance of the solutions' distance metric $\sigma(d_z) \leq \delta$, as

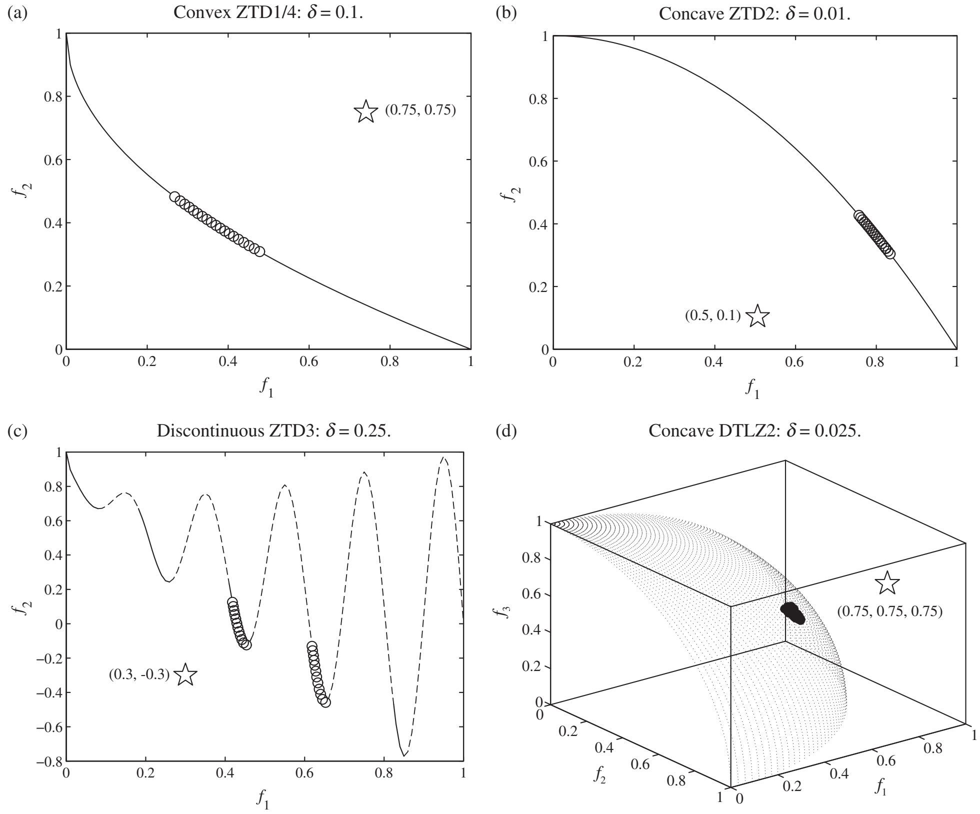

Figure 6. Illustration of the algorithm for multiobjective test functions.

illustrated in Figure 6. The extent of the solution spread is proportional to δ and evidently, as the value of δ increases, the influence of the location of $\mathbf{z}$ diminishes.

Identifying the most preferred solutions (for example from Figure 6) is highly dependent on the choice of the reference point. While the concept of the reference point may initially seem misleading, it in fact provides a very simple and intuitive method of articulating the preferred interests of the designer. Consider the three-objective DTLZ2 problem of Figure 6, where the boundaries of the Pareto front are in the unit hypercube $\mathbf{f} \in [0, 1]^3$. If one desires an absolutely equal weighting between all objectives then a reference point consisting of equal values should be considered, as illustrated in Figure 6. There are two possibilities to provide additional bias to any particular objective(s). The simplest approach to applying additional weighting to the objective f_3 would be to reduce the reference value for f_3, as illustrated in Figure 7(a). Alternatively it is possible to obtain a similar level of bias to a specific objective by relaxing the reference values of the other objective functions. This is illustrated in Figure 7(b), where the values of f_2 and f_3 are relaxed, naturally placing more emphasis on the objective f_1. Figure 7 demonstrates that by adding additional bias to any particular objective, the isolated preferred region shifts to the area which provides further improvement in the specific objective without affecting the compromise between other objectives.

In the context of an engineering design problem, if the original reference point (providing equal weighting) were representative of an existing design configuration, then a new reference point which emphasizes a specific design condition represents a *target* compromise where the designer is strictly interested in obtaining further improvement in that specific design objective. To illustrate

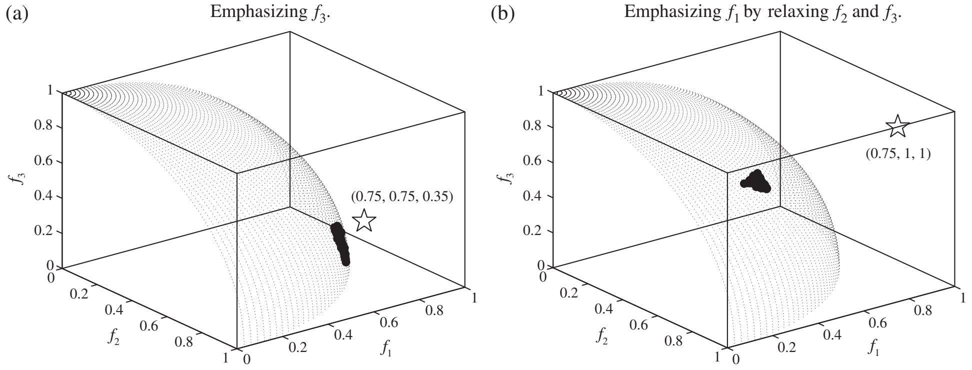

Figure 7. Manipulating the target compromise through adjustment of the reference point.

this concept, a computational experiment has been formulated to demonstrate the viability of the proposed method for the intended high-fidelity design application. The design space is analogous to that presented in Section 2, with the exception that the high-fidelity flow solver is replaced with a computationally inexpensive pressure-based Euler scheme. The multi-block grid is reconfigured to provide an approximate cell count of 10,000 elements based on the same O-grid topology. The Euler solver is still able to capture the important inviscid flow phenomena which are dependent on the relative position and interaction of the high-lift configuration elements. This experiment attempts to highlight the reference point guidance mechanism in converging to different preferred regions of the Pareto front.

The optimization problem introduced in Section 2 is reduced to a biobjective minimization problem for the functions f_1 and f_3. Within this flow regime drag is predominately a viscous effect, hence the objective function f_2 (which is a measure of the lift-to-drag ratio) has been omitted. For this experiment, two reference points are selected which focus on two different design philosophies. The first reference point $\mathbf{z}_1$ is based on the existing MDC 30P/30N configuration. The existing configuration is thus assumed to offer the preferred trade-off, and the algorithm will attempt to identify and exploit designs which offer improvement over the design objectives whilst maintaining a similar level of compromise. The second reference point $\mathbf{z}_2$ is modified to place higher priority on the approach condition f_1, both by emphasizing the f_1 reference value and by relaxing the f_3 reference value. It is immediately observed that designs guided by $\mathbf{z}_1$ favour the f_3 condition, whereas designs guided by $\mathbf{z}_1$ provide a more equal balance between the two design conditions.

4. Integrating the Kriging method

High-fidelity engineering design problems require the construction of an inexpensive surrogate model $\hat{f}$ that emulates the response of a function f. However, to construct a globally accurate surrogate of the original objective landscape is improbable due to the weakly correlated design space. It is more common to construct a global surrogate approximation based on a limited number of observations and then locally update the prediction accuracy of the surrogate as the search progresses towards promising areas of the design space (Forrester *et al.* 2008). For this reason, the Kriging method has received much interest in the optimization community, because it inherently considers confidence intervals of the predicted outputs. This method was first developed for the geostatistical field, but has recently received much interest by many researchers in engineering design (Jones 2001, Forrester *et al.* 2008).

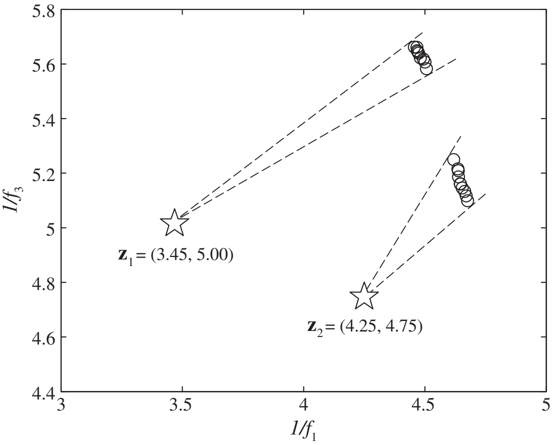

Figure 8. Identifying preferred designs on the Pareto front via different design philosophies.

4.1. *Kriging prediction*

The spatial arrangement of the initial observations is governed by the sampling array **X** of size (N, n) and the corresponding response **Y** of size $(N, 1)$:

$$\mathbf{X} = \{\mathbf{x}_1, \mathbf{x}_2, \ldots, \mathbf{x}_N\}\,; \quad \mathbf{Y} = \{y_1, y_2, \ldots, y_N\}\,. \tag{5}$$

The ordinary Kriging method predicts the response at an unobserved location **x** as

$$\hat{y}(\mathbf{x}) = \hat{\beta} + \mathbf{r}^{\mathrm{T}}\mathbf{R}^{-1}(\mathbf{Y} - \mathbf{1}\hat{\beta}), \tag{6}$$

where $\hat{\beta}$ is an approximation of the global mean value, **R** is the correlation matrix, **r** is the correlation vector, and **1** is a column vector of N elements of 1. The prediction accuracy of the Kriging model is updated by maximizing the concentrated natural log likelihood of the dataset **Y**, which is an n-variable single objective optimization problem, solved using a quasi-Newton method (Gano *et al.* 2006). The measure of uncertainty $\hat{y}$ in the prediction is estimated as

$$\hat{s}^2(\mathbf{x}) = \hat{\sigma}^2\left[1 - \mathbf{r}^{\mathrm{T}}\mathbf{R}^{-1}\mathbf{r} + \frac{(1 - \mathbf{1}^{\mathrm{T}}\mathbf{R}^{-1}\mathbf{r})^2}{\mathbf{1}^{\mathrm{T}}\mathbf{R}^{-1}\mathbf{1}}\right]. \tag{7}$$

The accuracy of the prediction $\hat{y}$ at the unobserved location **x** depends on the correlation distance with sample points **X**. The closer the location of **x** to the sample points, the more confidence in the prediction $\hat{y}(\mathbf{x})$. It is observed from Equation (7) that if $\mathbf{x} \subset \mathbf{X}$, then the measure of uncertainty $\hat{s}(\mathbf{x}) = 0$.

4.2. *Model management and particle screening*

The aim of a surrogate-assisted optimization framework is to use the precise objective functions and the inexpensive surrogate models cooperatively, in an effort to reduce the number of precise evaluations required for convergence. A procedure to manage and update the Kriging models is therefore required, in order to locally improve prediction accuracy in the preferred region of the design space.

After each population update, the non-dominated subset of **Y** is stored within the archive, which ensures that candidates for global leadership have been precisely evaluated (or with negligible prediction error) and, therefore, offer no false guidance to other particles. Adopting the concept of individual-based control (Jin 2005), Kriging predictions are then used to screen each candidate particle and subsequently flag them for precise evaluation or rejection. The Kriging model estimates a lower-confidence bound for the objective array as

$$\{\hat{f}_1(\mathbf{x}), \ldots, \hat{f}_m(\mathbf{x})\}_{\text{lb}} = \left[\left\{\hat{y}_1(\mathbf{x}) - \omega\hat{s}_1(\mathbf{x})\right\}, \ldots, \left\{\hat{y}_m(\mathbf{x}) - \omega\hat{s}_m(\mathbf{x})\right\}\right], \tag{8}$$

where $\omega = 2$ provides a 97% probability for $\hat{f}_{\text{lb}}(\mathbf{x})$ to be the lower bound value of $\hat{f}(\mathbf{x})$. An approximation to the reference point distance, $\hat{d}_z(\mathbf{x})$, can thus be obtained using Equation (4). This value, whilst providing a means of ranking each solution as a single scalar, also gives an estimate to the improvement that is expected from the solution. At time t, the archive member with the highest ranking according to Equation (4) is recorded as $d_{\min}$. The candidate $\mathbf{x}$ may then be accepted for precise evaluation, and subsequent admission into the archive if $\hat{d}_z(\mathbf{x}) < d_{\min}$. This criterion provides diversity exploring the design space, whilst balancing exploitation of the identified preferred region.

5. Numerical results

The algorithm described in the previous section is now combined with the high-fidelity RANS solver for an efficient design framework. The framework is applied to the re-design of the MDC 30P/30N configuration for robust aerodynamic performance, as described in Section 2. The authors, as the designers, select the reference point as the existing 30P/30N configuration in an attempt to improve on the performance characteristics whilst still maintaining a similar level of compromise between the design objectives. The solution spread is controlled by $\delta = 5 \times 10^{-3}$. The values of the reference point objective functions (as obtained by the flow solver) are $\mathbf{z} = [0.3338, 0.0182, 0.2361]$.

5.1. *Pre-optimization and variable screening*

Global Kriging models are constructed for the aerodynamic coefficients from a stratified sample of $N = 100$ design points based on a Latin hypercube sample (Mackay *et al.* 1979). This sampling plan size is considered sufficient in order to obtain sufficient confidence in the results of the subsequent design variable screening analysis. Whilst a larger sampling plan is essential to obtain an accurate global correlation, it is only of interest to quantify the elementary effect of each variable to the objective landscapes. The global Kriging models are initially trained via cross-validation. Illustrated in Figure 9 are the cross-validation curves for the Kriging models. The subscripts to the aerodynamic coefficients refer to the respective angles of incidence.

It is observed in Figures 9(a) and 9(b) that the constructed Kriging models for the aerodynamic coefficients at $\alpha = 8°$ are able to reproduce the training samples with sufficient confidence, recording error margin values of 3.21% and 3.83%, respectively. It is therefore apparent that the Kriging method is very adept at modelling complex landscapes represented by a limited number of precise observations. It is observed from Figure 9(c) that the largest error margin occurs in predicting the maximum lift (*i.e.* $C_{l_{19}}$), since at larger angles of incidence the nonlinear effects of flow separation and stall begin to dominate. In order to model a more correlated landscape, the sample from Figure 9(c) is conditioned, by eliminating all configurations which exhibit premature stall characteristics, such as unsteady flow. By conditioning the training sample, the design points are reduced to $N = 91$ and the error margin is reduced from 9.64 to 7.07%, which is highlighted in Figure 9(d).

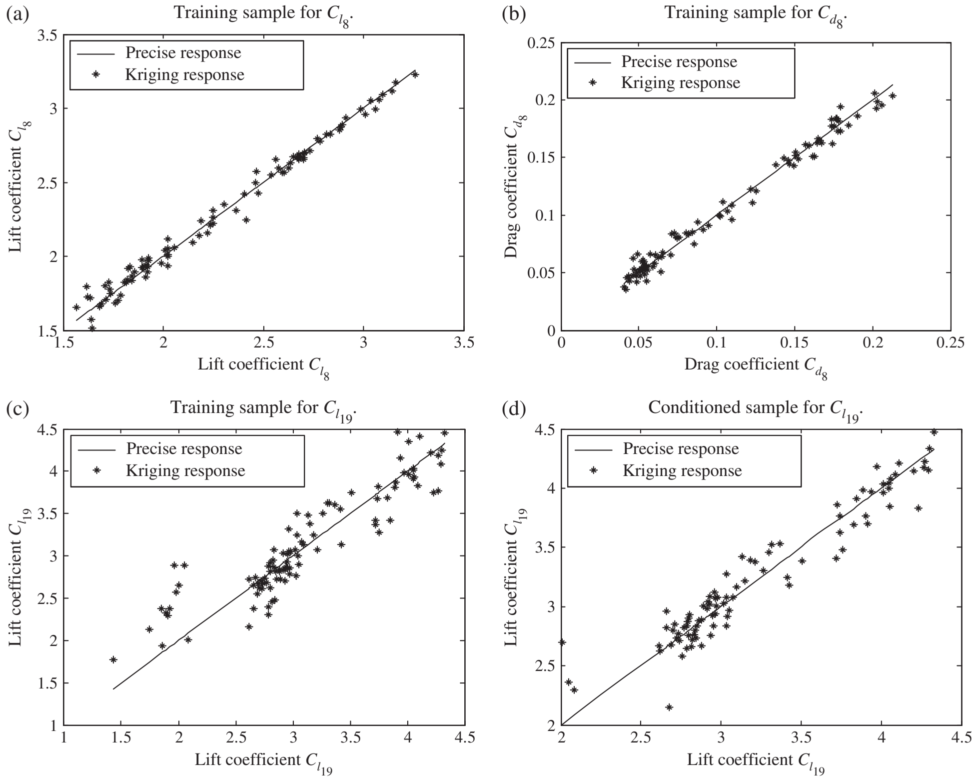

Figure 9. Cross-validation curves for the constructed Kriging models.

To investigate the elementary effect of each design variable on the metamodelled objective landscapes, a quantitative design space visualization technique is introduced. A popular method for designing preliminary experiments for design space visualization is the screening method developed by Morris (Morris 1991, Forrester *et al.* 2008). This algorithm calculates the elementary effect of a variable x_i and establishes its correlation with the objective space f as: (a) 'Negligible'; (b) 'Linear and additive'; (c) 'Nonlinear'; or (d) 'Nonlinear and/or involved in interactions with $x_j, \ldots$'. In plain terminology, the Morris algorithm measures the sensitivity of the ith variable to the objective landscape f. The design space S is restricted to an n-dimensional, p-level full factorial grid, where the normalized variable is

$$x_i \in \{0, 1/(p-1), 2/(p-1), \ldots, 1\}, \quad \text{for } i = 1, \ldots, n. \tag{9}$$

For a given baseline solution $\mathbf{x}$, let $d_i(\mathbf{x})$ denote the elementary effect of x_i, where

$$d_i(\mathbf{x}) = \frac{y(x_1, x_2, \ldots, x_{i-1}, x_i + \Delta, x_{i+1}, \ldots, x_n) - y(\mathbf{x})}{\Delta}, \tag{10}$$

where $\Delta = \xi/(p-1)$, $\xi \in \mathbb{N}^*$ is the elementary effect step length factor, and $\mathbf{x} \in S$ such that $x_i \leq 1 - \Delta$. Morris's screening method estimates the distribution of elementary effects of x_i over the design space S. If the variable x_i has a large central tendency μ_i, then this suggests an important influence on f. A large measure of spread σ_i suggests that either x_i is involved in interactions with other variables or is nonlinear with f. Campolongo *et al.* (2004) introduced a ranking measure μ^*, which is calculated from the mean of the distribution of the absolute values of the elementary effects, such that $\mu^* = \overline{|d_i(\mathbf{x})|}$. The proposed methodology addresses the misrepresentation of the magnitude of sensitivity, as a result of opposite signs of the elementary effects for a non-monotonic model (Khurana and Winarto 2010). To rank variables in order of influence or importance, the variable μ^* is used.

Figure 10 features the results obtained from the design variable screening study. It is immediately observed that in the approach condition (*i.e.* $\alpha = 8°$) the lift generated is almost entirely dependent on the position and orientation of the flap. This is expected, since the flap component is primarily responsible for increasing the loading of the high-lift configuration. The position of the slat has a more significant effect on the drag (and most importantly Δx_S) since this may effect the development of the confluent boundary layer and thus the shear stress distribution. The slat effects become much more significant at the maximum lift condition (*i.e.* $\alpha = 19°$). This is due to the fact that the slat component is primarily responsible for reducing the leading edge suction peak of the trailing elements, thus delaying flow separation. The slat influence is almost completely dictated by Δx_S and $\Delta\theta_S$ suggesting that Δy_S has no elementary effect on the maximum lift generated. Similar deductions can be made by examining the variable influence on d_z shown in Figure 10(d). The variable influence on d_z is case-specific and entirely dependent on the reference point chosen for the proposed optimization study. Since the value of d_z is a means of ranking the success of a multiobjective solution as one single scalar, variables may be ranked by influence, which is otherwise not possible when considering a multiobjective array. Preliminary conclusions to the priority weighting of the objectives to the reference point compromise can also be made. It is important to observe that slat effects are significant in the computation of d_z, which suggests that the maximum lift condition drives the design.

Table 2 consolidates the results of the design variable screening study, by ranking variable importance according to its influence on d_z. It is observed that the flap variables are the most significant variables, contributing to approximately 85% of the total influence. Once again, slat effects are almost entirely dependent on Δx_S and $\Delta\theta_S$, with Δy_S contributing to less than 1% of the total influence. In an industry setting, this result could be used to reduce the dimensionality of the problem by omitting the least influential variable Δy_S, which could potentially facilitate the

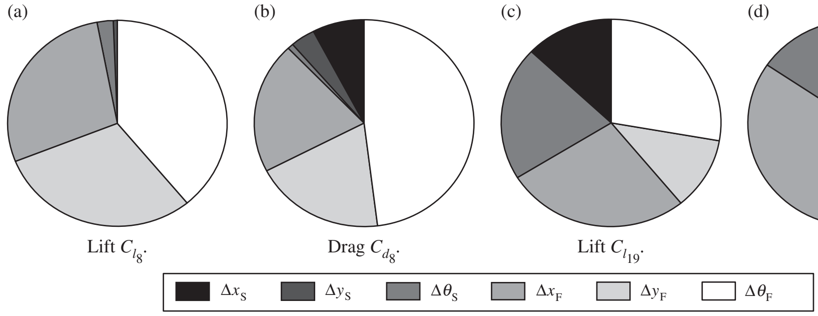

Figure 10. Variable influence on aerodynamic coefficients (subscripts refer to angles of incidence).

Table 2. Results of the design variable screening study and variable ranking.

Parameter	$\mu^*(C_{l_8})$ [%]	$\mu^*(C_{d_8})$ [%]	$\mu^*(C_{l_{19}})$ [%]	$\mu^*(d_z)$ [%]	Relative rank
Δx_S	<0.01	5.98	11.27	5.60	5
Δy_S	0.78	3.34	<0.01	0.34	6
$\Delta\theta_S$	2.32	0.69	19.00	9.58	4
Δx_F	30.76	25.20	27.42	31.84	1
Δy_F	33.03	19.71	13.45	23.34	3
$\Delta\theta_F$	33.12	45.08	28.84	29.28	2

optimization process. In this setting the variable Δy_S is not omitted since its negligible effect is a counter-intuitive result, and may be due to insufficient sampling. None the less, the true effect of Δy_S will be reconfirmed during the subsequent optimization and post-optimization processes.

5.2. *Optimization results*

A swarm population of 100 particles is initialized and flown to solve the optimization problem. The objective space is scaled such that there is no bias in the computation of the reference point distance metric. A computational budget of 250 evaluations is imposed. Based on the initial stratified sample of $N = 100$ design points, a further 150 precise evaluations are performed over $t \approx 70$ time-steps until the computational budget is breached. As shown in Figure 11(a), the largest number of update points are recorded during the initial explorative phase. As the preferred region is identified and the prediction error is reduced, the algorithm begins exploitation and the number of update points steadily reduces.

Figure 11(b) features the progress of the solution with minimum reference point distance $d_{\min}$ (referred to as the most preferred solution) as the number of precise evaluations escalates. The reference point criterion is shown to be proficient in filtering out poorer solutions during exploration and identifying the preferred region as only 50 evaluations are required to reach within 65% of the most preferred solution and an additional 50 evaluations to reach within 15%. Consistent improvement is then recorded due to exploitation of the preferred region until the search begins to converge after approximately 240 evaluations. The adept searching technique of the algorithm is further demonstrated in Figure 12(a) which features the 150 most recent solutions scheduled for precise evaluation. Attraction towards the preferred region dictated by the reference point is observed, which progressively becomes more focused and localized. Furthermore, few solutions appear to disturb the search direction of the algorithm, *i.e.* the trajectory of the search remains consistent. Hence, the reference point criterion proves to be very capable at filtering out solutions that do not reside within the preferred region. Featured in Figure 12(b) is the final set of 30 non-dominated solutions. The optimization framework was successful in obtaining solutions which exhibit improvement over all objectives compared with the reference point (*i.e.* the reference point is dominated).

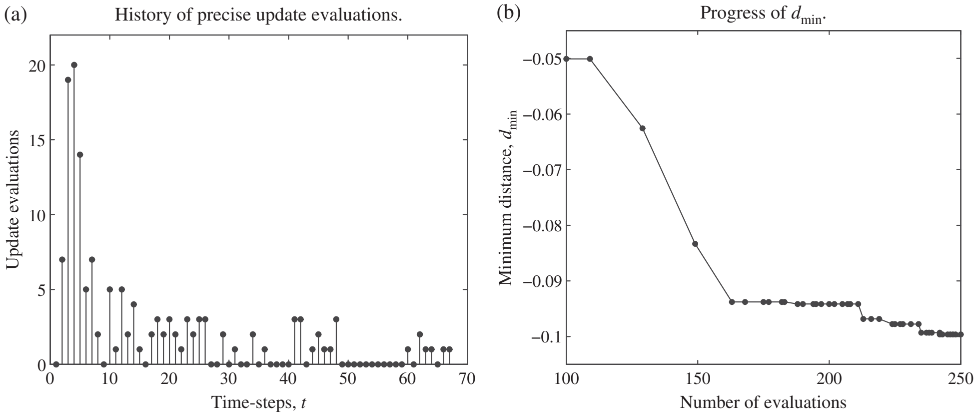

Figure 11. (a) History of precise update evaluations. (b) Progress of $d_{\min}$. Algorithm performance for the optimization case-study.

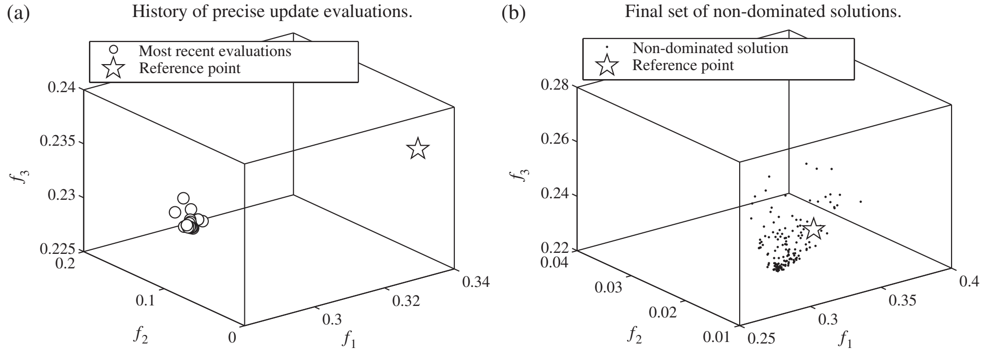

Figure 12. (a) History of precise update evaluations. (b) Final set of non-dominated solutions. Evaluations performed during the optimization study.

5.3. *Post-optimization and trade-off visualization*

The reference point distance also provides a feasible means of selecting the most appropriate solutions. For example, solutions may be ranked according to how well they represent the reference point compromise. To illustrate this concept, self-organizing maps (SOMs) are introduced to visualize the interaction of the objectives with the reference point compromise. Clustering SOM techniques are based on an unsupervised artificial neural network technique (Kohonen 1995) that can classify, organize and visualize large sets of data from a high-to-low dimensional space (Jeong *et al.* 2005; Khurana and Winarto 2010). A neuron used in this SOM analysis is associated with the weighted vector of objective inputs. Each neuron is connected to its adjacent neurons by a neighbourhood relation and forms a two-dimensional hexagonal topology. The SOM learning algorithm will attempt to increase the correlation between neighbouring neurons to provide a global representation of all solutions and their corresponding resemblance to the reference point compromise (Jeong *et al.* 2005).

The SOM analyses have been conducted using the software VISCOVERY SOMINE 5.2. The two-dimensionality of the charts is simply a means of clustering solutions to facilitate a qualitative visual analysis. Figure 13 features the post-optimization SOM trade-off study of the set of non-dominated solutions featured in Figure 12(b). The shading of the chart corresponds to the range of values for the specific quantity. The charts are clustered using four SOM-ward clusters, with priority to d_z. Each of the node values represent one possible non-dominated solution that the designer may select. The SOM chart coloured by d_z is a measure of how far a solution deviates from the preferred compromise. By following the other charts, the designer can visualize and

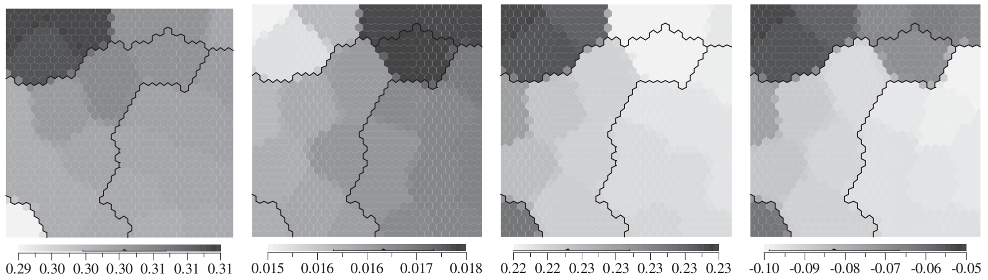

Figure 13. SOM charts to visualize optimal trade-offs between the design objectives.

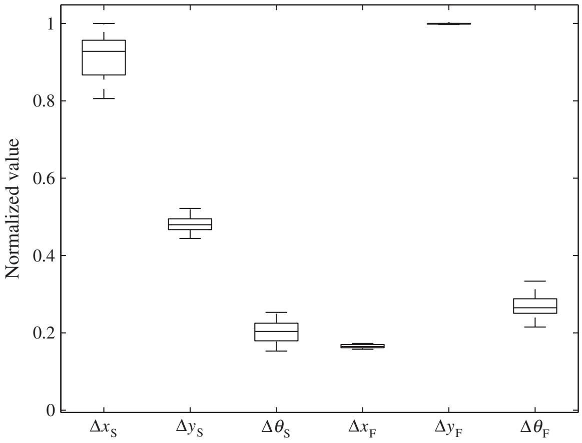

Figure 14. Box-plot of final non-dominated design variables.

relative priority of each objective function (and hence the design condition). It is immediately observed that the d_z chart most closely resembles the f_3 chart, indicating that this objective (*i.e.* maximum lift) has the highest priority. This complements the conclusion made from the design space screening analysis, discussed in Section 5.1. In subsequent optimization studies, to identify solutions which are more inclined to the other objectives, then the reference value for f_3 should be less stringent. Objectives f_1 and f_2 have a similar weighting and are within the middle bound of the identified objective ranges. Following these charts allows the designer to gain an understanding of the correlation between objectives f_1 and f_2 and the deviation from the preferred compromise.

To illustrate where the final solutions are located in the design space, a box-plot (see Figure 14) is generated of the non-dominated solutions from Figure 13. The design space is normalized to $[0, 1]^n$ for best visualization. It is observed from Figure 14 that the preferred region of the non-dominated front as dictated by the reference point compromise is well defined. A reduced flap rotation angle (increased flap deflection) increases the loading by effectively increasing the camber of the airfoil configuration. The reduced slat rotation angle may effectively reduce the magnitude of flow acceleration over the slat upper surface, injecting energy into the trailing element boundary layer whilst reducing the tendency of the flow to separate from the slat. The vertical translation of the flap Δy_F is at the upper bound, which could cause concern for system actuation. Both the horizontal translation of the slat and flap components are compacted such that they effectively reduce the chord, which is no doubt reflected in the increase of the lift-to-drag ratio over the reference point. The vertical translation of the slat Δy_S is the only variable shown which does not shift largely from the reference value (*i.e.* does not differ from the reference point 30P/30N configuration). This suggests that the variable already lies within the optimum region and thus does not have a significant impact on the dynamics of the swarm. This result coincides with the conclusion derived from the design variable screening analysis, discussed in Section 5.1. The optimization process could confidently be re-performed with Δy_S constant at the reference value, thereby alleviating some of the computational burden.

5.4. *Final designs*

Through visualization of the SOM charts, the trade-off relationships between solutions are quite clear despite the multi-dimensionality of the problem. Utilizing these charts, the designer may select the solution which best fits the target application. From the perspective of the present

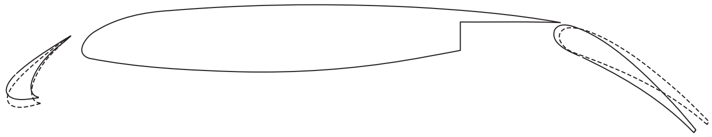

Figure 15. Comparison of the MDC 30P/30N configuration (- -) and the preferred solution (—).

Table 3. Performance of each configuration representing the most optimal values for each design condition.

Configuration	C_{l_8}	(C_l/C_d)	$C_{l_{19}}$
MDC 30P/30N	2.995	55.05	4.236
Preferred	3.286	58.92	4.423
minf_1	3.371	62.94	4.374
minf_2	3.194	64.84	4.335
minf_3	3.278	57.08	4.427

authors, the configuration that most resembles the compromise dictated by the reference point is considered the preferred solution. This corresponds to the solution which has the minimum distance metric $d_{\min}$. The variation in the component configuration is shown in Figure 15.

To facilitate the performance comparison between configurations, the objective functions are referred to by their aerodynamic coefficient equivalents. The values of the preferred configuration are listed in Table 3. Also tabulated are configurations which exhibit the most optimal value for the respective design conditions. The additional solutions provide an understanding to the extent of the preferred region. The preferred solution provides an approximate 9.7, 7.1 and 4.4% improvement over the reference 30P/30N configuration for the first, second and third design conditions, respectively. The preferred solution is clearly inclined towards the $C_{l_{19}}$ condition which is evident from the similarity to the minf_3 solution. This conclusion was also arrived at during the SOM post-optimization analysis discussed in Section 5.3.

6. Conclusion

In this article, an optimization framework has been introduced and applied to the aerodynamic design of a typical two-dimensional high-lift configuration. Qualitative and quantitative data mining tools are applied to visualize the design space and simplify a seemingly complex design problem. A surrogate-driven multiobjective particle swarm optimization algorithm is applied to navigate the design space to identify and exploit preferred regions of the Pareto frontier. The integration of all components of the optimization framework is entirely achieved through the use of a reference point distance metric which provides a scalar measure of the preferred interests of the designer. This effectively allows for the scale of the design space to be reduced, confining it to the interests reflected by the designer.

The developmental effort that is reported on here is to reduce the often prohibitive computational cost of multiobjective optimization to the level of practical affordability in computational aerodynamic design. The multiobjective re-design of a typical high-lift configuration has been considered by controlling the degree of motion of the forward and aft components in conjunction with a Reynolds-averaged Navier–Stokes flow solver. Kriging models were constructed based on a stratified sample of the design space. A pre-optimization visualization tool was then applied to screen variable elementary influence and quantify its relative influence to the preferred interests of the designer. Initial design-drivers were easily identified and an insight into the nonlinearity of the optimization landscape obtained. Optimization was achieved by driving a surrogate-assisted particle swarm towards a sector of special interest on the Pareto front which is shown to be an effective and efficient mechanism. It was observed that there is a distinct attraction towards the preferred region dictated by the reference point, which implies the reference point criterion is adept at filtering out solutions which will disrupt or deviate from the optimal search path.

Non-dominated solutions which provide significant improvement over the reference geometry were identified within the imposed computational budget, and are clearly reflective of the preferred interest. A post-optimization data-mining tool was finally applied to facilitate a qualitative trade-off visualization study. This analysis provides an insight into the relative priority of each objective and their influence on the preferred compromise. Conclusions complement the findings of the pre-optimization screening study. Further studies could also evaluate the influence of visualization tools to facilitate the optimization process by omitting variables which have a negligible influence and assist in making informed decisions which can potentially minimize the scale of the optimization problem.

Acknowledgements

The authors would like to gratefully acknowledge the Program Development Company, Inc., for kindly providing a GRIDPRO™ licence for the duration of this research. Special thanks go to Lev Lafayette and Craig West from the Victorian Partnership for Advanced Computing. This work would not have been possible without their efforts. The authors would also like to gratefully acknowledge Tanja Zauner of Viscovery Software GmbH for kindly providing a VISCOVERY SOMINE 5.2 licence for this research.

References

Carrese, R., *et al.*, 2011a. Benefits of incorporating designer preferences within a multi-objective airfoil design framework. *Journal of Aircraft*, 48 (3), 832–844.

Carrese, R., *et al.*, 2011b. Swarm heuristic for identifying preferred solutions in surrogate-based multi-objective engineering design. *American Institute of Astronautics and Aeronautics Journal*, 52 (7), 1437–1449.

Clerc, M., and Kennedy, J., 2002. The particle swarm – explosion, stability, and convergence in a multidimensional complex space. *IEEE Transactions on Evolutionary Computation*, 6 (1), 58–73.

Deb, K., 2001. *Multi-objective optimization using evolutionary algorithms*. Chichester, UK: Wiley.

Deb, K., *et al.*, 2005. Scalable test problems for evolutionary multi-objective optimization. *In*: *Evolutionary Multiobjective Optimization (EMO): Advanced Information and Knowledge Processing*. Heidelberg: Springer-Verlag, 105–145.

Deb, K. and Sundar, J., 2006. Reference point based multi-objective optimization using evolutionary algorithms. *In*: *Genetic and evolutionary computation conference (GECCO)*, 8–12 July, Seattle, WA. New York: ACM Press, 635–642.

Fonseca, C.M., and Fleming, P.J., 1995. An overview of evolutionary algorithms in multiobjective optimization. *Evolutionary Computation*, 3 (1), 1–16.

Fonseca, C.M., and Fleming, P.J., 1998. Multiobjective optimization and multiple constraint handling with evolutionary algorithms – Part I: A unified formulation. *IEEE Transactions on Systems, Man and Cybernetics – Part A: Systems and Humans*, 28 (1), 26–37.

Forrester, A., Sóbester, A., and Keane, A., 2008. *Engineering design via surrogate modelling: a practical guide*. Chichester, UK: Wiley.

Gano, S., *et al.*, 2006. Update strategies for Kriging models used in variable fidelity optimization. *Structural and Multidisciplinary Optimization*, 32 (4), 345–383.

Garner, L., Meredith, P.T., and Stoner, R.C., 1991. Areas for CFD development as illustrated by transport aircraft applications. AIAA Paper 91-1527.

Greenman, R.M. and Roth, K.R., 1999. High-lift optimization design using neural networks on a multi-element airfoil. *Journal of Fluids Engineering*, 121 (2), 434–440.

Jeong, S., Chiba, K., and Obayashi, S., 2005. Data mining for aerodynamic design space. *Journal of Aerospace Computing, Information, and Communication*, 2 (11), 452–469.

Jin, Y., 2005. A comprehensive survey of fitness approximation in evolutionary computation. *Soft Computing*, 9 (1), 3–12.

Jones, D.R., 2001. A taxomony of global optimization methods based on response surfaces. *Journal of Global Optimization*, 21 (4), 345–383.

Kanazaki, M., Jeong, S., and Yamamoto, K., 2006. High-lift system optimization based on the Kriging model using a high-fidelity flow solver. *Transactions of the Japan Society for Aeronautical and Space Sciences*, 49 (165), 169–174.

Keane, A.J. and Nair, P.B., 2005. *Computational approaches for aerospace design: the pursuit of excellence*. Chichester, UK: Wiley.

Kennedy, J. and Eberhart, R.C., 2001. *Swarm intelligence*. San Francisco, CA: Morgan Kaufmann.

Khurana, M.S. and Winarto, H., 2010. Development and validation of an efficient direct numerical optimisation approach for airfoil shape design. *The Aeronautical Journal*, 114 (1160), 611–628.

Kim, S., Alonso, J.J., and Jameson, A., 2004. Multi-element high-lift configuration design optimization using viscous continuous adjoint method. *Journal of Aircraft*, 41 (5), 1082–1097.

Kohonen, T., 1995. *Self-organizing maps*. Heidelberg: Springer-Verlag.

Mackay, M.D., Beckman, R.J., and Conover, W.J., 1979. A comparison of three methods for selecting values of input variables in the analysis of output from a computer code. *Technometrics*, 21 (2), 239–245.

Marler, R.T. and Arora, J.S., 2004. Survey of multi-objective optimization methods for engineering. *Structural and Multidisciplinary Optimization*, 26 (6), 369–395.

Morris, M.D., 1991. Factorial sampling plans for preliminary computational experiments. *Technometrics*, 33 (2), 161–174.

Obayashi, S. and Sasaki, D., 2003. Visualization and data mining of Pareto solutions using self-organizing map. *In*: *Proceedings of the second international conference on evolutionary multi-criterion optimization*, 8–11 April, Faro, Portugal. Berlin: Springer, 796–809.

Quagliarella, D. and Vicini, A., 2001. Viscous single and multicomponent airfoil design with genetic algorithms. *Finite Elements in Analysis and Design*, 37 (5), 365–380.

Rachmawati, L. and Srinivasan, D., 2006. Preference incorporation in multi-objective evolutionary algorithms: a survey. *In*: *IEEE congress on evolutionary computation*, 16–21 July, Vancouver, Canada. New York: IEEE Press, 635–642.

Rogers, S.E., *et al.*, 1994. A comparison of turbulence models in computing multi-element airfoil flows. AIAA Paper 94-0291.

Rumsey, C.L., *et al.*, 1998. Prediction of high-lift flows using turbulence closure models. *American Institute of Astronautics and Aeronautics Journal*, 36 (5), 765–774.

Rumsey, C.L. and Ying, S.X., 2002. Prediction of high lift: review of present CFD capability. *Progress in Aerospace Sciences*, 38 (2), 145–180.

Saltelli, A., *et al.*, 2004. *Sensitivity analysis in practice. A guide to assessing scientific models*. Chichester, UK: Wiley.

Sierra, M.R. and Coello, C.A.C., 2006. Multi-objective particle swarm optimizers: a survey of the state-of-the-art. *International Journal of Computational Intelligence Research*, 2 (3), 287–308.

Smith, A.M., 1975. High-lift aerodynamics. *Journal of Aircraft*, 12 (6), 501–530.

Spalart, P.R. and Allmaras, S.R., 1992. A one-equation turbulence model for aerodynamic flows. AIAA Paper 92-0439.

Trelea, I.C., 2003. The particle swarm optimization algorithm: convergence analysis and parameter selection. *Information Processing Letters*, 85 (6), 317–325.

van Dam, C.P., 2002. The aerodynamic design of multi-element high-lift systems for transport airplanes. *Progress in Aerospace Sciences*, 38 (2), 101–144.

Vatsa, V.N., *et al.*, 1994. Multi-block structured grid approach for solving flows over complex aerodynamic configurations. AIAA Paper 94-0655.

Wickramasinghe, U.K. and Li, X., 2008. Integrating user preferences with particle swarms for multi-objective optimization. *In*: *Genetic and evolutionary computation conference (GECCO)*, 12–16 July, Portland, OR. New York: ACM Press, 745–752.

Ying, S.X., *et al.*, 1999. Investigation of confluent boundary layers in high-lift flows. *Journal of Aircraft*, 36 (3), 550–562.

Zitzler, E., Deb, K., and Thiele, L., 2000. Comparison of multiobjective evolutionary algorithms: empirical results. *Evolutionary Computation*, 8 (2), 173–195.